Cancer Research

Investigation of Optical Coherence Microelastography as a Method to Visualize Cancers in Human Breast Tissue

Brendan F. Kennedy[1], Robert A. McLaughlin[1], Kelsey M. Kennedy[1], Lixin Chin[1], Philip Wijesinghe[1], Andrea Curatolo[1], Alan Tien[2], Maxine Ronald[3], Bruce Latham[4], Christobel M. Saunders[2,3], and David D. Sampson[1,5]

Abstract

An accurate intraoperative identification of malignant tissue is a challenge in the surgical management of breast cancer. Imaging techniques that help address this challenge could contribute to more complete and accurate tumor excision, and thereby help reduce the current high reexcision rates without resorting to the removal of excess healthy tissue. Optical coherence microelastography (OCME) is a three-dimensional, high-resolution imaging technique that is sensitive to microscale variations of the mechanical properties of tissue. As the tumor modifies the mechanical properties of breast tissue, OCME has the potential to identify, on the microscale, involved regions of fresh, unstained tissue. OCME is based on the use of optical coherence tomography (OCT) to measure tissue deformation in response to applied mechanical compression. In this feasibility study on 58 *ex vivo* samples from patients undergoing mastectomy or wide local excision, we demonstrate the performance of OCME as a means to visualize tissue microarchitecture in benign and malignant human breast tissues. Through a comparison with corresponding histology and OCT images, OCME is shown to enable ready visualization of features such as ducts, lobules, microcysts, blood vessels, and arterioles and to identify invasive tumor through distinctive patterns in OCME images, often with enhanced contrast compared with OCT. These results lay the foundation for future intraoperative studies. *Cancer Res; 75(16); 3236–45. ©2015 AACR.*

Introduction

Breast cancer has the second highest mortality rate of all cancers in women (1). It is estimated that in 2014 more than 40,000 people died from the disease in the United States, accounting for 15% of all cancer-related female deaths (1). Surgical excision of the tumor is a critical factor in the treatment of breast cancer. In breast-conserving surgery, the primary aims are to remove all malignant tissue while ensuring a good cosmetic outcome (2). During surgery, the decision of which tissue to excise is guided by a combination of preoperative and intraoperative imaging (3), macroscopic examination (4) and manual palpation. Final margin evaluation is only available postoperatively from histopathologic analysis, often performed days after the surgery. If this analysis indicates that tumor is present close to, or at, the boundary of excised tissue (5), a secondary surgery is often performed to remove additional tissue, and additional radiotherapy is prescribed. It has been reported that approximately 30% to 60% of patients undergoing breast-conserving surgery require a second surgery (6). Such additional surgery has a negative impact on the patient (7), places a significant burden on the healthcare system (8), and increases the likelihood of complications such as wound infection (9). Subsequent boost radiotherapy increases healthcare costs and has accompanying complications (10). Intraoperative diagnostic techniques, such as frozen section and imprint cytology, are currently used to aid in margin assessment. However, these techniques are time consuming and less accurate than postoperative histopathologic analysis, and reported positive margin rates using these techniques are greater than 20% (11). To address this issue, a number of optical imaging techniques have been proposed, including optical coherence tomography (OCT; ref. 12) and Raman spectroscopy (13).

We report on an optical imaging technique with the potential to provide intraoperative high-resolution assessment of tumor margins. Optical coherence microelastography (OCME) is an emerging member of a suite of techniques, known collectively as elastography, that use variations in tissue stiffness to form images (14). In elastography, a mechanical load is imparted to a tissue and the resulting local motion in the tissue is detected using imaging (15). A mechanical property or parameter is then computed and mapped into an image (elastogram), enabling visualization of tissue stiffness. Variants of elastography based on ultrasound (16) and MRI (17) have been developed as diagnostic tools to evaluate suspicious breast lesions, and a number of large clinical studies have been performed (18–20). However, the

[1]Optical+Biomedical Engineering Laboratory, School of Electrical, Electronic and Computer Engineering, The University of Western Australia, Crawley, Western Australia, Australia. [2]School of Surgery, The University of Western Australia, Crawley, Western Australia, Australia. [3]Breast Clinic, Royal Perth Hospital, Perth, Western Australia, Australia. [4]PathWest, Perth, Western Australia, Australia. [5]Centre for Microscopy, Characterization and Analysis, The University of Western Australia, Crawley, Western Australia, Australia.

Note: Supplementary data for this article are available at Cancer Research Online (http://cancerres.aacrjournals.org/).

Corresponding Author: Brendan F. Kennedy, The University of Western Australia, 35 Stirling Highway, Crawley, WA 6009, Australia. Phone: 618-6488-4746; Fax: 618-6488-1319; E-mail: brendan.kennedy@uwa.edu.au

doi: 10.1158/0008-5472.CAN-14-3694

relatively low spatial resolution of existing elastography techniques may limit their suitability for intraoperative tumor margin assessment. OCME achieves microscale resolution by using OCT as the imaging modality (21–24). OCT may be described as the optical analog to ultrasonography (25). The detection of the echo time delays of scattered light waves, rather than of scattered sound waves, conveys to it a spatial resolution of 1 to 10 μm but only to a depth of 1 to 2 mm in breast tissue. OCME and related optical elastography techniques are being developed for a number of applications, most notably in ophthalmology and cardiology, as well as in cancer (23).

A number of studies have evaluated OCT for imaging of excised human breast tissue (26–31) and lymph nodes (32–34). These studies have indicated that OCT may be used to visualize breast microarchitecture, but that it is difficult to distinguish tumor from stroma in OCT images. OCT contrast between tumor and stroma is based on differences in their respective optical properties (26–31). The contrast in OCME images (microelastograms), alternatively, is provided by differences in tissue mechanical properties. As the stiffness variations in breast tissue are correlated with both anatomical structures and pathologic state (35), OCME has the potential to be used to more accurately identify tumor and complement the contrast provided by OCT (24).

The objective of this study is to evaluate the potential of OCME for imaging breast microarchitecture. To achieve this, we use an OCME system developed in our laboratory to image freshly excised benign and malignant human breast tissue. OCME is compared with coregistered hematoxylin and eosin (H&E)–stained histology, and OCT. The results demonstrate that OCME can be used to visualize features, including ducts, lobules, microcysts, blood vessels, and arterioles, and to distinguish regions of invasive tumor from a background of mature stroma. Overlaid OCME and OCT images highlight the complementary nature of the mechanical and optical contrast of breast tissue. This study paves the way for future intraoperative studies on the use of OCME in the assessment of tumor margins, with the potential to eventually reduce the existing high reexcision rates in breast-conserving surgery.

Materials and Methods

OCT acquires images by illuminating a biological sample with a focused beam of nonionizing, near-infrared light, and detecting the component of this light that is backscattered. Backscattering from different depths within the tissue is separated through a process referred to as low-coherence interferometry, providing a one-dimensional depth scan (A-scan) of the tissue at a specific location. An image is formed by acquiring a sequence of these scans by scanning the focused beam across the sample (B-scan). A three-dimensional (3D) data volume, a C-scan, is constructed by acquiring a sequence of adjacent B-scans. Elastography is performed by minutely varying the mechanical load on the tissue successively from B-scan to B-scan. Additional technical detail is provided in the following sections.

OCME system

A portable OCME imaging system was used in this study (Fig. 1), comprising a spectrometer-based, Fourier-domain OCT system and a mechanical loading apparatus. The light source is a superluminescent diode (Superlum, Ireland) with an optical

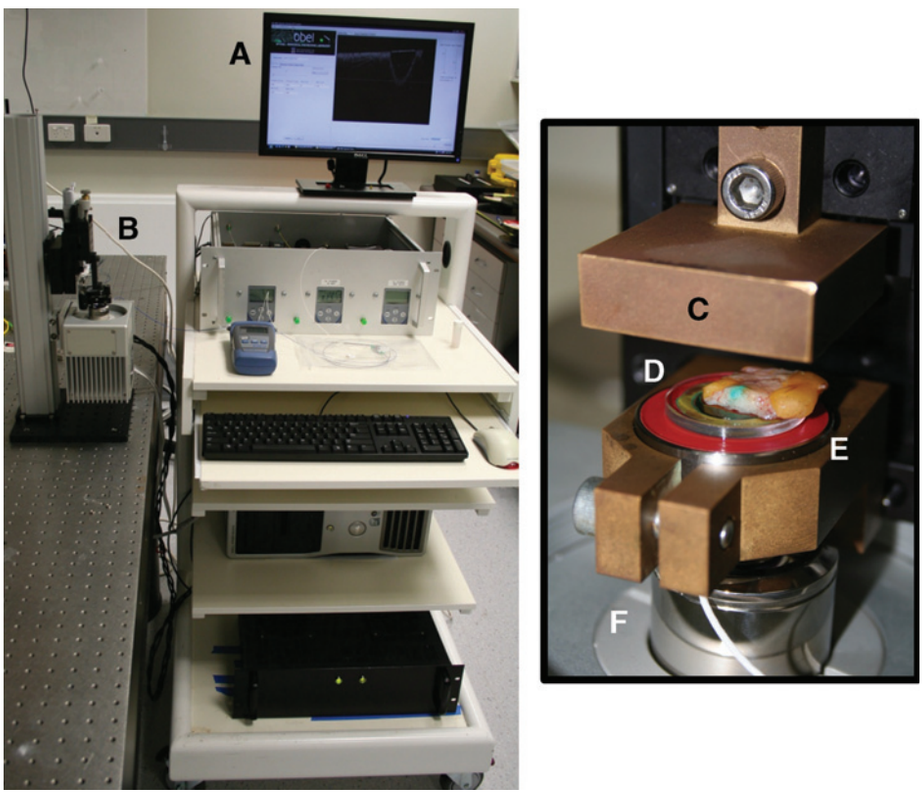

Figure 1.
Photographs of the OCME imaging system (left) and a sample in position on the imaging stage (right). A, OCT system. B, mechanical loading apparatus and the imaging stage. C, rigid plate used to preload the sample. D, human breast tissue sample placed on the imaging window. E, annular piezoelectric transducer used to compress the sample during OCME imaging. F, imaging lens.

spectrum centered at a wavelength of 835 nm and with a bandwidth (full-width at half-maximum) of 50 nm. To optimize the sensitivity to displacement of the tissue, the interferometer is configured in common-path mode (36), in which the reference reflector is provided by the interface between a glass window and the tissue surface. The OCT axial and transverse resolutions were measured to be 8 and 11 μm (in air), respectively. The optical power incident on the sample was approximately 7 mW. The sensitivity of the system was measured to be 102 decibels at an exposure time of 36 μs. The exposure times used to obtain the results presented in this article were in the range of 3 to 15 μs and the period of each A-scan was 100 μs. To acquire B-scans and C-scans, the light beam was scanned in both transverse (x and y) dimensions using a pair of galvanometer mirrors (Scanlab). For OCME imaging, the system acquired B-scans and C-scans in 0.1 s and approximately 16 minutes, respectively. 3D datasets were acquired with dimensions ($x \times y \times z$) up to $10 \times 10 \times 2.25$ mm, comprising 1,000 A-scans in each B-scan and 10,000 B-scans in each C-scan. The data were acquired using a custom-made software package written in the C++ language. Signal processing of the raw data was performed in Matlab (Mathworks, v2012b).

Mechanical loading

To impart a mechanical load to the tissue, the glass imaging window was fixed to an annular piezoelectric transducer (Piezomechanik), providing for mechanical loading and optical imaging from the same side of the sample (Fig. 1; ref. 37). To ensure even contact with the window, before imaging, the sample was preloaded from the nonimaging side by displacing a rigid brass plate 0.5 to 1.5 mm beyond the point of initial contact with the sample. The preload corresponds to a bulk strain (change in sample thickness over its initial thickness) in the range of 0.1 to 0.3. It is important to note that this is not the strain that is measured in OCME. During imaging, the transducer imparted an additional, much smaller mechanical load by displacing the tissue surface by up to a maximum of 2.2 μm. It is the strain resulting from this micron-scale actuation that is measured in OCME. The transducer was driven at a frequency of 5 Hz and was synchronized with the OCT acquisition such that consecutive B-scans were acquired in the loaded then unloaded state.

Acquisition parameters and signal processing

Tissue displacement was estimated using 3D, phase-sensitive OCT (23). To ensure consecutive B-scan pairs were correlated, oversampling was used in the y-direction such that B-scans were spaced at 1-μm intervals (24). This ensured that the phase difference between each pair of B-scans was proportional to the axial displacement of the tissue. Weighted averaging and phase unwrapping were used to improve the precision and dynamic range of measurable displacements (24). To provide mechanical contrast, 3D microelastograms were generated from the 3D displacement map by estimating the local strain at each location in the sample using a weighted-least squares linear regression algorithm described previously (38). Local strain is defined as the change of displacement over an axial depth (38). In this study, the local strain was estimated over an axial range of 100 μm, which defined the axial resolution of the OCME system. The transverse (x and y) resolution matched that of the underlying OCT system (11 μm). For a sample undergoing uniaxial compression and under the assumption that stress is uniformly distributed throughout a sample, negative local strain is indicative of tissue stiffness; that is, for a given load, softer regions undergo higher local strain than stiffer regions.

Imaging protocol

Informed consent was obtained from patients and the study approved by the Human Research Ethics Committee of Royal Perth Hospital, Perth, Western Australia. Fifty-eight samples were imaged, taken from 31 patients undergoing a lumpectomy, mastectomy, or mastectomy with axillary clearance. After excision, a fresh tissue sample was dissected for scanning, with approximate dimensions ($x \times y \times z$) of $1.5 \times 1.5 \times 0.5$ cm. Samples were kept hydrated in saline until imaging, which occurred within 4 hours of excision. Each sample was mechanically loaded and imaged, as described above. After imaging, samples were fixed in 10% neutral-buffered formalin, embedded in paraffin, sectioned, and stained with H&E following the standard histopathology protocols used at Royal Perth Hospital. The H&E-stained sections were digitally micrographed using an automated system (ScanScope, Leica Biosystems) and manually coregistered with the corresponding *en face* microelastograms and *en face* OCT images using in-house viewing software. All images presented correspond to depth locations either 50 or 300 μm from the tissue surface. Interpretation of histology was performed by an experienced pathologist (B. Latham). The *en face* OCT image corresponding most closely to each microelastogram was chosen from the set of OCT images within the axial range of the microelastogram (100 μm). In Figs. 1–5, the maximum field-of-view in microelastograms and OCT images is 10×10 mm. In Figs. 6 and 7, a larger field-of-view ($\sim 20 \times \sim 20$ mm) was obtained by mosaicking four 10×10 mm scans acquired from partially overlapping square regions of the sample. Microelastograms are presented on a linear dimensionless scale using pseudo-color (in millistrain, mε, that is, length change per unit length $\times 10^{-3}$) and OCT images are presented on a logarithmic decibel scale using a grayscale colormap. Negative strain in a microelastogram corresponds to strain in the same direction as the applied load, and positive strain corresponds to strain acting in the opposite direction. Because a sample undergoes uniaxial compression in OCME, predominantly negative local strain is expected; however, the mechanical heterogeneity of breast tissue is such that regions of positive local strain are also observed. The mechanisms by which positive local strain can occur are described in detail in the Supplementary Material.

Fused OCT/OCME images were generated by first segmenting out the adipose tissue from the microelastograms using image processing software (GNU Image Manipulation Program, v2.8.2), because OCT is effective in distinguishing this tissue type from other solid tissues due to its distinct optical properties. The remaining OCME data are overlaid on the OCT image. To accentuate the OCME contrast in the fused images, the OCT image transparency is set to 20%.

Results

In the following, we present results of imaging normal and various types of malignant breast tissue. Each result comprises H&E histology, the corresponding *en face* microelastogram and the *en face* OCT image. Figure 2 shows two representative examples of benign breast tissue, in which various characteristic features may be observed. Figure 2A–C shows epithelial hyperplasia characterized by increased cell density in the terminal duct lobular

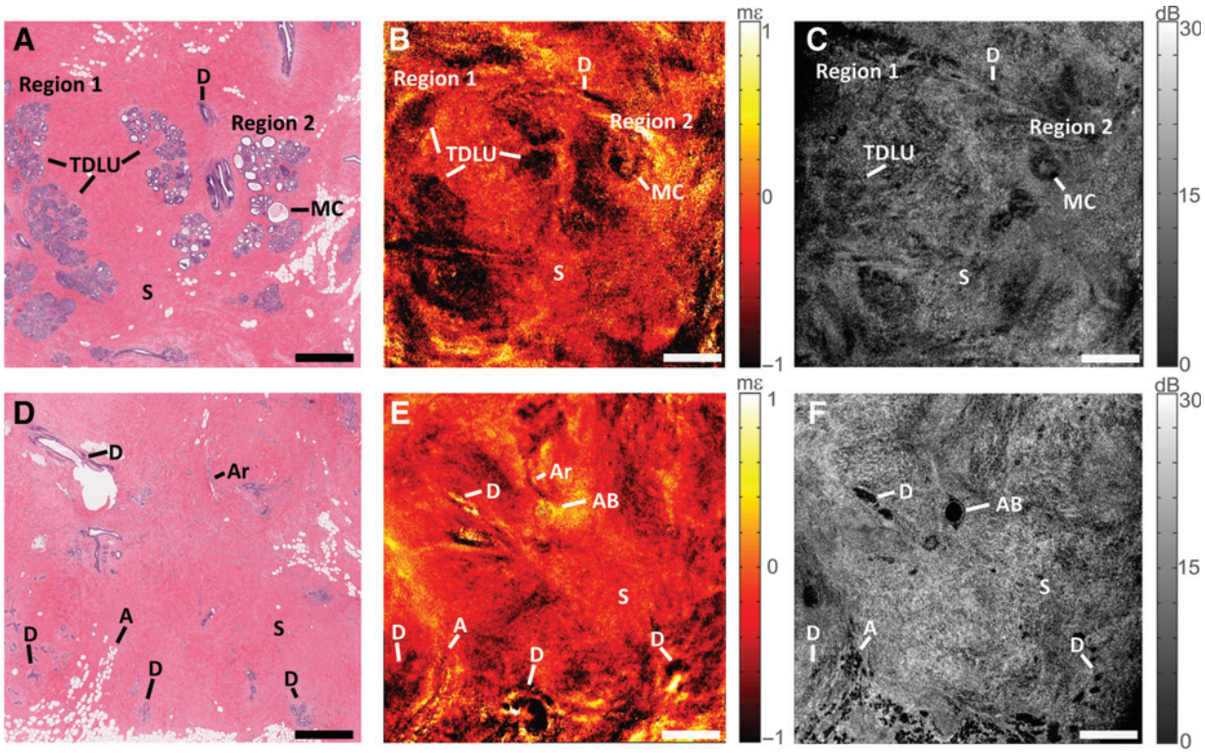

Figure 2.
Benign breast tissue. A–C, epithelial hyperplasia. D–F, benign atrophic breast. A and D, histology. B and E, *en face* microelastograms at depths of approximately 300 and 50 μm, respectively. C and F, corresponding *en face* OCT images. A, adipose tissue; AB, air bubble; Ar, arterioles; D, duct; MC, microcyst; S, mature stroma; and TDLU, terminal duct lobular unit. mε, millistrain; dB, decibels. Scale bars, 1 mm.

units (TDLU) and ducts (D). The region labeled "Region 1" shows atypical ductal hyperplasia and that labeled "Region 2" shows microcyst formation and mild epithelial hyperplasia. Figure 2D–F shows benign atrophic breast tissue, characterized by atrophic ducts and increased interlobular fibrosis. The microelastograms in Fig. 2B and E demonstrate the effectiveness of OCME in delineating features of benign breast tissue. In these microelastograms, TDLUs, ducts and arterioles (Ar) appear as regions of higher negative local strain than surrounding mature stroma (S), suggesting they are of lower stiffness. Mature stroma presents as a uniform texture, indicating mechanical uniformity. In both microelastograms, there is a well-defined boundary between TDLUs, ducts, arterioles, and mature stroma. In several of these features, positive local strain is present around the feature boundary, which accentuates the feature contrast. Intralobular features are also visible in microelastograms. In Fig. 2B, mechanical heterogeneity is visible within the TDLUs in Region 1, likely arising from a distinct mechanical response from intralobular stroma and acini. Several of the same features are visible in the OCT images in Fig. 2C and F, particularly TDLUs and ducts, which manifest as regions of lower optical backscatter than surrounding mature stroma, as reported previously (26, 27). The characteristic honeycomb structure of adipose tissue is also visible, particularly in Fig. 2F. In summary, Fig. 2 demonstrates that multiple features of benign breast tissue are readily identified in microelastograms, and the contrast is complementary to that provided by OCT.

Figure 3 demonstrates the capacity to use OCME to distinguish malignant from benign breast tissue. Mucinous carcinoma, a relatively uncommon invasive carcinoma seen in 2% to 3% of all cases, is typified by nests of tumor cells (T) interspersed between regions of mucin (M; Fig. 3A). The microelastogram shown in Fig. 3B provides clear delineation between the malignant tissue and the surrounding mature stroma (S). Similarly to Fig. 2B and E, stroma appears as a region of uniform local strain. In the region of malignancy, the distinct mechanical properties of tumor and mucin result in highly heterogeneous local strain. The malignant tissue is characterized by intermixed regions of negative and positive local strain, allowing the boundary of the malignant tissue to be identified. In the OCT image (Fig. 3C), there is visible contrast between the tumor and mucin, with the mucin appearing as a dark region, indicating lower optical backscatter. However, the boundary between the tumor and surrounding mature stroma is difficult to discern, as these tissue types have similar optical backscattering properties, highlighting the importance of the additional tissue contrast provided by OCME.

Figures 4 and 5 present representative examples of the most common breast malignancy, invasive ductal carcinoma. In Fig. 4, the central region consists of mature stroma (S) and is surrounded by tumor (Fig. 4A). Above the stroma lies a region of invasive tumor (T), comprising densely packed tumor cells. A number of malignant lobules and ducts, exhibiting characteristics of ductal carcinoma *in situ* (DCIS) and comedo necrosis, also surround the central region of mature stroma. The corresponding microelastogram (Fig. 4B) demonstrates that OCME can distinguish malignant tissue from stroma. The heterogeneity within the involved lobules gives rise to a complex strain pattern, with higher strain

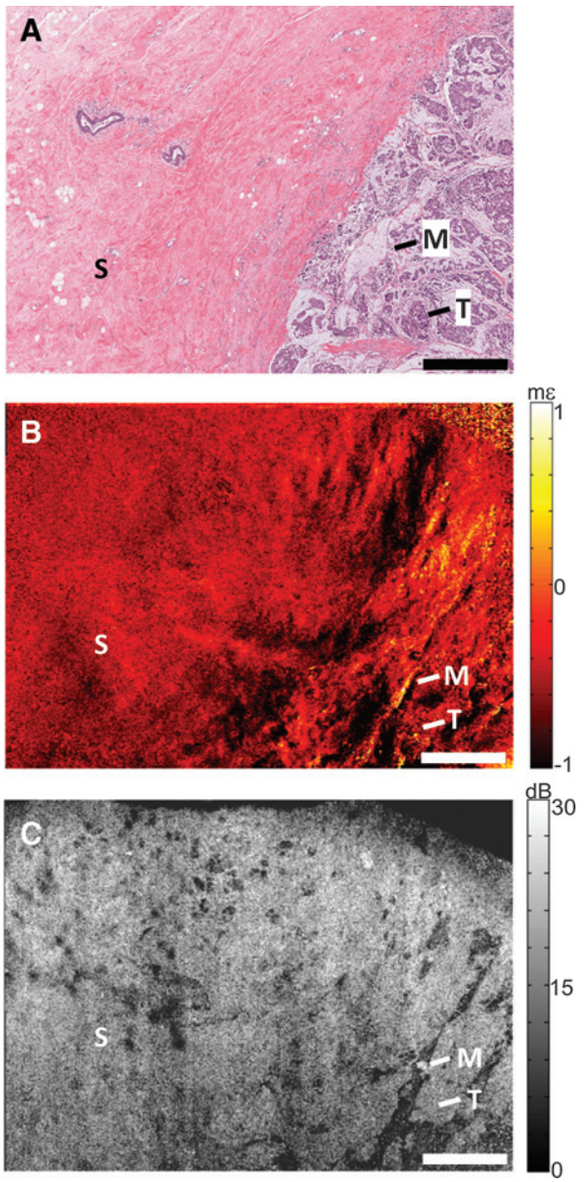

Figure 3.
Mucinous carcinoma. A, histology. B, *en face* microelastogram at approximately 50 μm depth. C, corresponding *en face* OCT image. M, mucin; S, mature stroma; T, tumor; mε, millistrain; dB, decibels. Scale bars, 1 mm.

heterogeneity than is visible in the benign lobules shown in Fig. 2. Similarly to Figs. 2 and 3, the central stromal region of the microelastogram presents a uniform texture. The invasive tumor above the mature stroma presents as a region of high negative local strain, indicating that it is softer than the mature stroma. In the corresponding OCT image (Fig. 4C), the lobules and tumor are readily distinguished from the mature stroma, and individual adipose cells are resolved within the stroma.

In Fig. 5, a second example of invasive ductal carcinoma is shown, in which the central region consists of mature stroma (S; Fig. 5A). The stroma is surrounded by invasive tumor (T) comprising infiltrating nests of tumor cells that invoke a desmoplastic stromal response. In the microelastogram (Fig. 5B), as seen in Figs. 2–4, uniform strain is visible in the mature stroma. By comparison, the regions with infiltrating tumor present as a highly heterogeneous texture in the microelastogram, characterized by adjacent regions of negative and positive local strain. This heterogeneity is caused by differences in the mechanical properties and structure between the nests of tumor cells and the surrounding immature desmoplastic stroma. The distinct textures in the microelastogram allow the regions of infiltrating tumor to be identified. In the OCT image (Fig. 5C), strands of immature desmoplastic stroma appear as brighter regions (high backscatter) interspersed with darker regions (low backscatter) corresponding to nests of tumor cells. Comparing the contrast provided by OCME and OCT in Fig. 5, similarly to Fig. 3, the border between benign and malignant tissue is more readily identified with OCME.

Figures 2–5 suggest that OCME and OCT are complementary in identifying morphologic features within freshly excised, unstained breast tissue. The results presented here suggest that the mechanical contrast in microelastograms can distinguish regions of invasive tumor from uninvolved mature stroma, whereas the optical contrast in OCT images readily delineates adipose tissue. To better utilize these complementary sources of

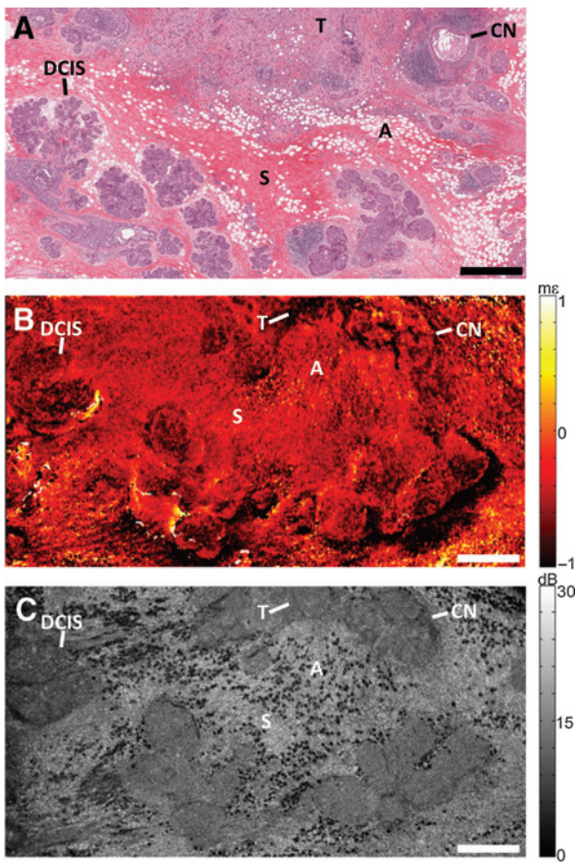

Figure 4.
Invasive ductal carcinoma. A, histology. B, *en face* microelastogram at approximately 50 μm depth. C, corresponding *en face* OCT image. A, adipose tissue; CN, comedo necrosis; DCIS, ductal carcinoma *in situ*; S, mature stroma; T, tumor; mε, millistrain; dB, decibels. Scale bars, 1 mm.

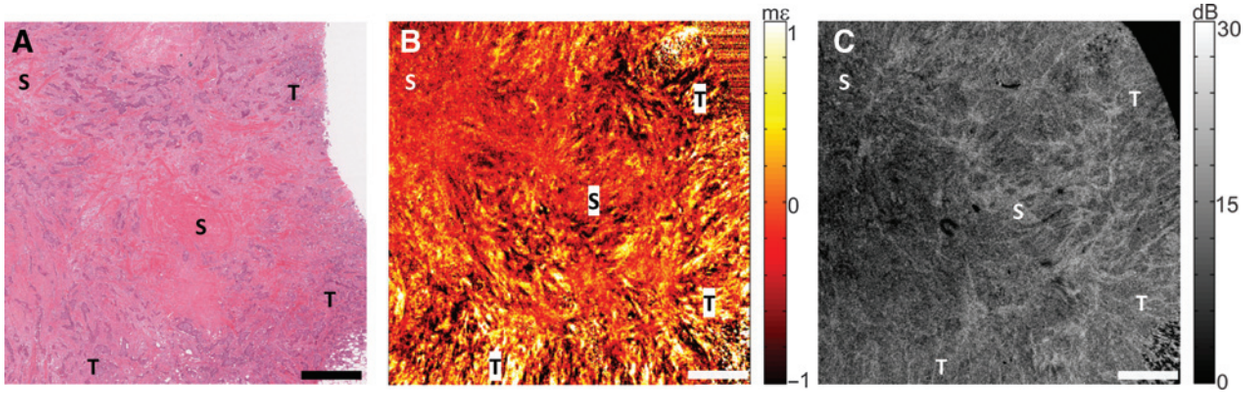

Figure 5.
Invasive ductal carcinoma. A, histology. B, *en face* microelastogram at approximately 50 μm depth. C, corresponding *en face* OCT image. S, mature stroma; T, tumor; mε, millistrain; dB, decibels. Scale bars, 1 mm.

contrast, Figs. 6 and 7 show fused images in which the non-adipose sections of the microelastogram are overlaid on the OCT image. In addition, Figs. 6 and 7 extend the field of view to ∼20 × ∼20 mm by mosaicking four overlapping square portions of a square image. Figure 6 shows an example of invasive ductal carcinoma surrounded by adipose tissue (A). In the top half of the histology image (Fig. 6A), a region of mature stroma (S) is present. A number of features of normal breast tissue, such as ducts (D) and blood vessels (V), are interspersed within the stroma. The bottom half of Fig. 6A shows a region of invasive tumor (T). The radially advancing edge of the tumor is characterized by nests of tumor cells surrounded by immature desmoplastic stroma advancing into adipose tissue. In the microelastograms, these two regions are distinct. The uniform texture of the mature stroma in the microelastogram, visible in the fused image (Fig. 6B), is similar to that in Figs. 2–5. Ducts and blood vessels present as regions of high negative local strain. The local strain in areas of invasive malignancy is highly heterogeneous, similar to that shown in Fig. 5, and characteristic of malignant cells compromising the structure of the healthy tissue. By comparison, the OCT image (Fig. 6C) delineates the adipose tissue, but provides little contrast between the tumor and mature stroma. Figure 6D–I shows magnified images of the histology, fused microelastogram/OCT and OCT images in involved and uninvolved tissues, corresponding to the locations indicated by the blue and black arrows in Fig. 6A–C, and highlight the additional contrast achieved by incorporating OCME.

Figure 7 shows a second example of a fused microelastogram and OCT image of a sample containing invasive ductal carcinoma. From the histology image (Fig. 7A), the central region consists of mature stroma (S) with invasive tumor (T) advancing radially into

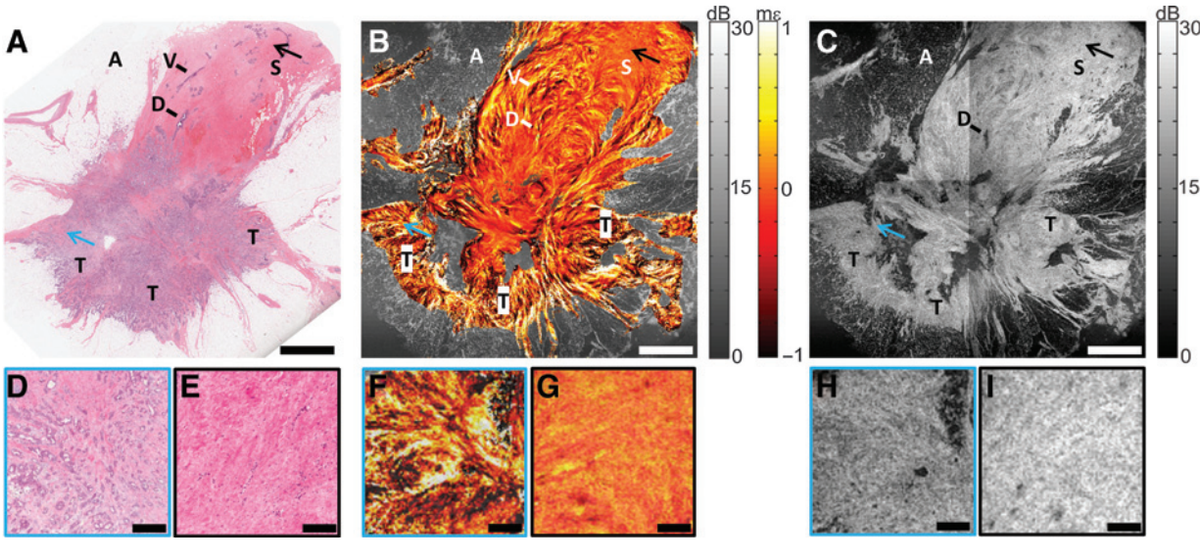

Figure 6.
Invasive ductal carcinoma. A, histology. B, *en face* fused OCT image and microelastogram at approximately 50 μm depth, showing OCME in color and OCT in gray scale. C, corresponding *en face* OCT image. A, adipose tissue; D, duct; S, mature stroma; T, tumor; and V, blood vessel. Blue arrows in A–C indicate the region of tumor corresponding to D, F, and H. Black arrows in A–C indicate the region of mature stroma corresponding to E, G, and I. dB, decibels; mε, millistrain. Scale bars in A–C, 3 mm; scale bars in D–I, 0.5 mm.

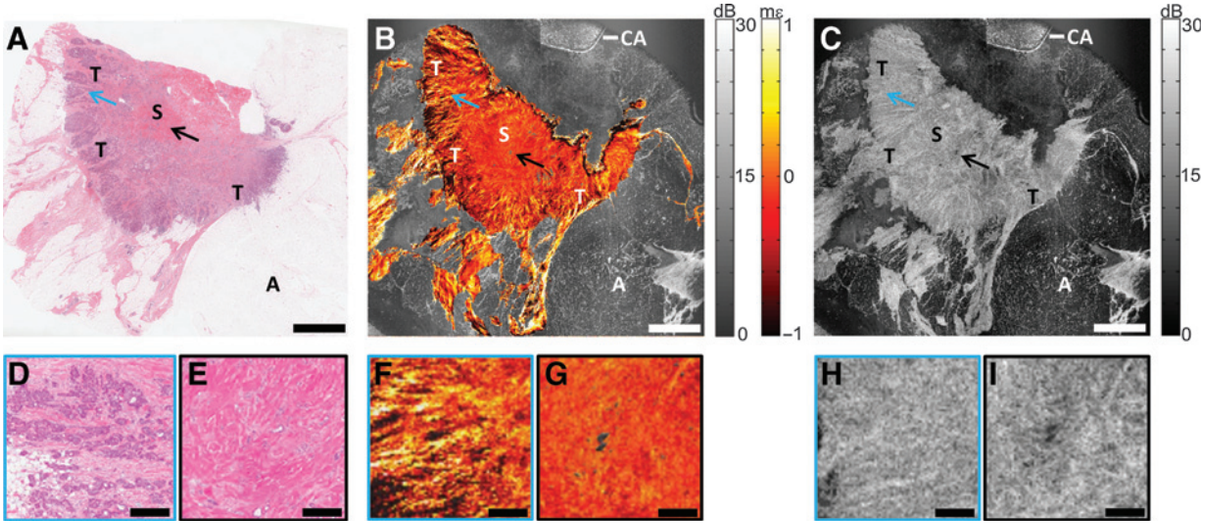

Figure 7.
Invasive ductal carcinoma. A, histology. B, *en face* fused OCT image and microelastogram, showing OCT in gray scale and OCME in color at approximately 50 μm depth. C, corresponding *en face* OCT image. A, adipose tissue; CA, contact artifact; S, mature stroma; and T, tumor. Blue arrows in A–C indicate the region of tumor corresponding to D, F, and H. Black arrows in A–C indicate the region of mature stroma corresponding to E, G, and I. dB, decibels; mε, millistrain. Scale bars in A–C, 3 mm; scale bars in D–I, 0.5 mm.

adipose tissue (A). In the fused image (Fig. 7B), the microelastogram shows the characteristic patterns observed in Figs. 2–6. The central stromal region corresponds to a uniform strain pattern, suggesting that it is mechanically homogeneous. The advancing edge of the tumor, comprising nests of tumor cells in demosplastic stroma, corresponds to the heterogeneous strain pattern also observed in the invasive tumors shown in Figs. 5 and 6. Similarly to Fig. 6C, OCT readily distinguishes the adipose tissue but provides low contrast between tumor and stroma (Fig. 7C). The much higher contrast between benign and malignant tissue in the microelastogram is highlighted in the magnified images in Fig. 7D–I, which correspond to the locations indicated by the blue and black arrows in Fig. 7A–C.

Discussion and Conclusion

In this article, we have presented representative microelastograms selected from the 58 fresh, unstained breast tissue samples scanned. In benign and malignant tissue, we observe lobules, ducts, microcysts, blood vessels, and arterioles. These features exhibit high negative local strain, enabling them to be distinguished from surrounding mature stroma. In areas of invasive malignancy, often characterized by nests of tumor cells interspersed within immature desmoplastic stroma, microelastograms display a heterogeneous pattern, characterized by regions of negative and positive local strain (Figs. 5–7). Mature stroma manifests as regions of comparatively uniform negative local strain (Figs. 2–7). Positive local strain acts to accentuate feature contrast in areas of high mechanical heterogeneity, for example, around the boundaries of features and in areas of malignancy where tumor cells are interspersed with desmoplastic stroma (24). Positive local strain is described in greater detail in the Supplementary Material. These distinct strain patterns provide the basis for OCME to be used to distinguish between benign mature stroma and tissue with invasive malignancy.

The results presented here also demonstrate that OCME provides contrast that is additional and complementary to that provided by OCT imaging alone. Whereas OCT readily distinguishes mature stroma and tumor from adipose in tissue, microelastograms exhibit high contrast between tissues with similar optical backscattering properties, such as at the boundary between mature stroma and invasive tumor. We have demonstrated that this complementarity may be effectively used through image fusion. In so doing, we are following the well-established precedents of image fusion set in medical imaging techniques such as MRI, X-ray CT, and PET (39).

The high degree of heterogeneity in the mechanical properties of invasive tumor observed in this study is consistent with laboratory studies of breast tissue surfaces conducted on the nano- to microscale using atomic force microscopy (40, 41). These studies have reported that cancer cells are typically softer than normal breast cells and that stroma, often present in malignant lesions, is typically stiffer than cancer cells. This combination results in substantial mechanical heterogeneity on the microscale probed by OCME (41). Macroscopically, the elevated stiffness often associated with tumors, and sensed during palpation, is dominated by the stromal response to malignancy, rather than by the tumor cells (41).

Similarly to previously reported feasibility studies of OCT on breast tissue (26, 27, 29), the diagnostic accuracy of OCME has not been reported here, as the goal of this study is to establish the contrast provided by OCME in breast tissue. Given the promise of the results presented here, subsequent work will focus on determining the sensitivity and specificity of the presence of malignant tumor in tumor margins. Such a study will require OCME to be performed on the intact tumor mass, as has been reported for OCT imaging of tumor margins (12). The data acquired in this feasibility study will serve as a training set for pathologists before their participation in blind studies to assess the diagnostic accuracy of OCME. To attempt such an

analysis on the microelastograms acquired thus far is premature for several reasons. First, in this feasibility study, we have imaged small tissue volumes (~1.5 × 1.5 × 0.5 cm) dissected mainly from mastectomy specimens. Our study was performed on samples dissected from locations deep within the tumor and far from the tumor boundary. Thus, although very encouraging results have been obtained, the imaging performance at the tumor boundary needs to be established on much larger lumpectomy specimens, which we are indeed currently investigating. Second, as we have so far imaged tissue excised from 31 patients, we do not expect to have enough data to report statistically significant values of sensitivity and specificity. For an expected sensitivity and specificity of 90%, and assuming 25% of specimens have either DCIS or invasive ductal carcinoma within 2 mm of the tissue boundary (based on an internal audit performed in two major public hospital breast units in Western Australia in 2009), we require $n = 138$ to determine sensitivity and $n = 46$ to determine specificity to a precision of 10% (95% confidence interval; ref. 42).

The ultimate goal of this work is to scan the boundaries of the excised tumor intraoperatively and to provide the surgeon with an assessment of tumor margins within several minutes of excision. Translation of OCME to intraoperative analysis of tumor margins presents additional challenges not encountered in the present study. For example, surgical artifacts such as cauterized tissue and blood could degrade microelastogram quality by attenuating the optical beam as it penetrates the tissue surface. Such issues have been addressed in OCT of tumor margins and were found not to interfere with the ability to assess the margin (12). To remove residual surface blood in that study, saline was used successfully to irrigate the excised tissue before imaging. As OCME relies on OCT to measure tissue motion, adopting the same practice should remove such artifacts.

A further barrier to intraoperative translation is the imaging speed. With the OCME system reported here, 10 × 10 mm *en face* images were acquired in approximately 16 minutes. Our group has recently demonstrated higher speed acquisition, enabling 10 × 10 mm *en face* images to be acquired in approximately 20 seconds (43). Using this technique, in combination with the mosaicking used in Figs. 6 and 7, 30 × 30 mm *en face* images could be generated in approximately 3 minutes. This timeframe compares favorably with existing intraoperative techniques, such as frozen section, which typically takes approximately 25 minutes (44). In addition, recent advances in OCT technology have enabled data acquisition speeds of >1,000,000 A-scans per second, permitting volume acquisitions in <1 second (45), suggesting that entire lumpectomy samples could feasibly be scanned in <1 minute. However, we note that further technical development of the rapid acquisition technique (43) is required to achieve microelastograms of the quality presented in Figs. 2–7.

OCME is one of a number of emerging optical elastography techniques (23). These techniques can be classified according to the method used to introduce a mechanical load and include compression (24), shear wave (46), and magnetomotive techniques (47). Compressive loading is used in OCME (24). In shear wave OCE, a pulsed or periodic load generates surface/shear waves that are detected using OCT (46). In magnetomotive OCE, magnetic nanoparticles are distributed in the tissue and actuated using an external magnetic field to produce localized displacements (47). Each variant of optical elastography would appear to have particular advantages suited to specific applications. For example, wave-based, non-contact techniques providing absolute quantification of tissue stiffness appear to be most suited to measuring delicate, relatively homogeneous tissues, such as the cornea (46). For intraoperative margin assessment, where rapid assessment of highly heterogeneous tissues over relatively large areas is required, but quantification of absolute stiffness may not be needed, compression techniques, such as OCME, appear to be more suitable (23).

In common with all compression-based elastography techniques (15), mechanical contrast in OCME is obtained by measuring local strain at each location in the sample at the expense of spatial resolution in the direction of strain measurement. To estimate local strain, the slope of axial displacement is measured over a depth range of 100 μm, representing in our case a 12.5× degradation in resolution compared with the native OCT axial resolution. In the transverse plane (x- and y-dimensions), by contrast, OCME retains the OCT resolution (11 μm in our case). Despite the inherent reduction in axial resolution, the results presented here demonstrate that OCME is readily able to distinguish microarchitecture within breast tissue.

Beyond intraoperative assessment of excised tumor, OCME may be suitable in other clinical scenarios, mirroring the proposed applications of OCT in breast cancer imaging. For example, development of a handheld OCME probe, similar to commercially available handheld OCT probes, would enable intraoperative assessment of the tumor cavity. Needle-based elastography probes could guide both tumor excision and needle biopsies by providing high-resolution imaging deep within the breast (48). OCME could also be used to assess axillary lymph node involvement in breast cancer metastasis, and initial results have been reported (24). Beyond breast cancer, a recent article has proposed the use of a closely related optical elastography technique in prostate cancer (49).

In conclusion, the visualization of mechanical contrast in breast tissue provided by OCME represents a new mechanism for the identification of malignant tissue on the microscale, with the potential to provide a new means of intraoperative assessment of tumor margins. In this first major study, we have performed a detailed analysis of representative examples of OCME of human breast tissue and demonstrated strong correspondence between microelastograms and coregistered histology. The study also reveals the additional and complementary nature of OCME contrast compared with that of OCT. These results lay the foundation for future evaluation of OCME as an intraoperative technique for the assessment of tissue excised during breast-conserving surgery.

Disclosure of Potential Conflicts of Interest

No potential conflicts of interest were disclosed.

Authors' Contributions

Conception and design: B.F. Kennedy, C.M. Saunders, D.D. Sampson
Development of methodology: B.F. Kennedy, R.A. McLaughlin, K.M. Kennedy, L. Chin, A. Curatolo, B. Latham, C.M. Saunders, D.D. Sampson
Acquisition of data (provided animals, acquired and managed patients, provided facilities, etc.): B.F. Kennedy, R.A. McLaughlin, K.M. Kennedy, L. Chin, P. Wijesinghe, A. Curatolo, A. Tien, M. Ronald, B. Latham, C.M. Saunders
Analysis and interpretation of data (e.g., statistical analysis, biostatistics, computational analysis): B.F. Kennedy, R.A. McLaughlin, K.M. Kennedy, L. Chin, P. Wijesinghe, B. Latham, C.M. Saunders, D.D. Sampson

Writing, review, and/or revision of the manuscript: B.F. Kennedy, R.A. McLaughlin, K.M. Kennedy, L. Chin, P. Wijesinghe, B. Latham, C.M. Saunders, D.D. Sampson
Administrative, technical, or material support (i.e., reporting or organizing data, constructing databases): B.F. Kennedy, R.A. McLaughlin
Study supervision: B.F. Kennedy, D.D. Sampson

Acknowledgments

The authors acknowledge the facilities, and the scientific and technical assistance of the Australian Microscopy and Microanalysis Research Facility at the Centre for Microscopy, Characterization and Analysis, The University of Western Australia, a facility funded by the University, State and Commonwealth Governments.

Grant Support

This research was supported in part by grants and fellowships from the Australian Research Council, the National Health and Medical Research Council (Australia), the National Breast Cancer Foundation (Australia), the Raine Medical Research Foundation, Cancer Council Western Australia, a scholarship from the Gledden Trust of The University of Western Australia, and a Scholarship for International Research Fees, The University of Western Australia.

The costs of publication of this article were defrayed in part by the payment of page charges. This article must therefore be hereby marked *advertisement* in accordance with 18 U.S.C. Section 1734 solely to indicate this fact.

Received December 16, 2014; revised June 3, 2015; accepted June 14, 2015; published OnlineFirst June 29, 2015.

References

1. American Cancer Society: cancer facts and figures. 2014. Available from: http://www.cancer.org/research/cancerfactsstatistics/cancerfactsfigures2014.
2. Fisher B, Anderson S, Bryant J, Margolese RG, Deutsch M, Fisher ER, et al. Twenty-year follow-up of a randomized trial comparing total mastectomy, lumpectomy, and lumpectomy plus irradiation for the treatment of invasive breast cancer. New Engl J Med 2002;347:1233–41.
3. Pleijhuis RG, Graafland M, de Vries J, Bart J, de Jong JS, van Dam GM. Obtaining adequate surgical margins in breast-conserving therapy for patients with early-stage breast cancer: current modalities and future directions. Ann Surg Oncol 2009;16:2717–30.
4. Balch GC, Mithani SK, Simpson JF, Kelley MC. Accuracy of intraoperative gross examination of surgical margin status in women undergoing partial mastectomy for breast malignancy. Am Surgeon 2005;71:22–8.
5. Dillon MF, Hill AD, Quinn CM, McDermott EW, O'Higgins N. A pathologic assessment of adequate margin status in breast-conserving therapy. Ann Surg Oncol 2006;13:333–9.
6. Waljee JF, Hu ES, Newman LA, Alderman AK. Predictors of re-excision among women undergoing breast-conserving surgery for cancer. Ann Surg Oncol 2008;15:1297–303.
7. Okamura M, Yamawaki S, Akechi T, Taniguchi K, Uchitomi Y. Psychiatric disorders following first breast cancer recurrence: prevalence, associated factors and relationship to quality of life. Jpn J Clin Oncol 2005;35:302–9.
8. Hurley S, Huggins R, Snyder R, Bishop J. The cost of breast cancer recurrences. Brit J Cancer 1992;65:449–55.
9. Tran C-L, Langer S, Broderick-Villa G, DiFronzo LA. Does reoperation predispose to postoperative wound infection in women undergoing operation for breast cancer? Am Surg 2003;69:852–6.
10. Wazer DE, DiPetrillo T, Schmidt-Ullrich R, Weld L, Smith T, Marchant D, et al. Factors influencing cosmetic outcome and complication risk after conservative surgery and radiotherapy for early-stage breast carcinoma. J Clin Oncol 1992;10:356–63.
11. Cabioglu N, Hunt KK, Sahin AA, Kuerer HM, Babiera GV, Singletary SE, et al. Role for intraoperative margin assessment in patients undergoing breast-conserving surgery. Ann Surg Oncol 2007;14:1458–71.
12. Nguyen FT, Zysk AM, Chaney EJ, Kotynek JG, Oliphant UJ, Bellafiore FJ, et al. Intraoperative evaluation of breast tumor margins with optical coherence tomography. Cancer Res 2009;69:8790–6.
13. Haka AS, Volynskaya Z, Gardecki JA, Nazemi J, Lyons J, Hicks D, et al. *In vivo* margin assessment during partial mastectomy breast surgery using raman spectroscopy. Cancer Res 2006;66:3317–22.
14. Parker K, Doyley M, Rubens D. Imaging the elastic properties of tissue: the 20 year perspective. Phys Med Biol 2011;56:R1–29.
15. Ophir J, Cespedes I, Ponnekanti H, Yazdi Y, Li X. Elastography: a quantitative method for imaging the elasticity of biological tissues. Ultrason Imaging 1991;13:111–34.
16. Itoh A, Ueno E, Tohno E, Kamma H, Takahashi H, Shiina T, et al. Breast disease: clinical application of US elastography for diagnosis. Radiology 2006;239:341–50.
17. McKnight AL, Kugel JL, Rossman PJ, Manduca A, Hartmann LC, Ehman RL. MR elastography of breast cancer: preliminary results. Am J Roentgenol 2002;178:1411–7.
18. Chang JM, Moon WK, Cho N, Kim SJ. Breast mass evaluation: factors influencing the quality of US elastography. Radiology 2011;259:59–64.
19. Berg WA, Cosgrove DO, Doré CJ, Schäfer FK, Svensson WE, Hooley RJ, et al. Shear-wave elastography improves the specificity of breast US: the BE1 multinational study of 939 masses. Radiology 2012;262:435–49.
20. Cosgrove DO, Berg WA, Doré CJ, Skyba DM, Henry J-P, Gay J, et al. Shear wave elastography for breast masses is highly reproducible. Eur Radiol 2012;22:1023–32.
21. Schmitt J. OCT elastography: imaging microscopic deformation and strain of tissue. Opt Express 1998;3:199–211.
22. Nahas A, Bauer M, Roux S, Boccara AC. 3D static elastography at the micrometer scale using full field OCT. Biomed Opt Express 2013;4:2138–49.
23. Kennedy BF, Kennedy KM, Sampson DD. A review of optical coherence elastography: fundamentals, techniques and prospects. IEEE J Sel Top Quant 2014;20:1–17.
24. Kennedy BF, McLaughlin RA, Kennedy KM, Chin L, Curatolo A, Tien A, et al. Optical coherence micro-elastography: mechanical-contrast imaging of tissue microstructure. Biomed Opt Express 2014;5:2113–24.
25. Huang D, Swanson EA, Lin CP, Schuman JS, Stinson WG, Chang W, et al. Optical coherence tomography. Science 1991;254:1178–81.
26. Hsiung PL, Phatak DR, Chen Y, Aguirre AD, Fujimoto JG, Connolly JL. Benign and malignant lesions in the human breast depicted with ultrahigh resolution and three-dimensional optical coherence tomography. Radiology 2007;244:865–74.
27. Zhou C, Cohen DW, Wang YH, Lee HC, Mondelblatt AE, Tsai TH, et al. Integrated optical coherence tomography and microscopy for *ex vivo* multiscale evaluation of human breast tissues. Cancer Res 2010;70:10071–9.
28. Assayag O, Antoine M, Sigal-Zafrani B, Riben M, Harms F, Burcheri A, et al. Large field, high resolution full-field optical coherence tomography: a preclinical study of human breast tissue and cancer assessment. Technol Cancer Res T 2013;13:455–68.
29. Patel R, Khan A, Quinlan R, Yaroslavsky AN. Polarization-sensitive multimodal imaging for detecting breast cancer. Cancer Res 2014;74:4685–93.
30. Scolaro L, McLaughlin RA, Kennedy BF, Saunders CM, Sampson DD. A review of optical coherence tomography in breast cancer. Photonics Lasers Med 2014;3:225–40.
31. South FA, Chaney EJ, Marjanovic M, Adie SG, Boppart SA. Differentiation of *ex vivo* human breast tissue using polarization-sensitive optical coherence tomography. Biomed Opt Express 2014;5:3417–26.
32. Luo W, Nguyen FT, Zysk AM, Ralston TS, Brockenbrough J, Marks DL, et al. Optical biopsy of lymph node morphology using optical coherence tomography. Technol Cancer Res T 2005;4:539–47.
33. McLaughlin RA, Scolaro L, Robbins P, Hamza S, Saunders C, Sampson DD. Imaging of human lymph nodes using optical coherence tomography: potential for staging cancer. Cancer Res 2010;70:2579–84.
34. John R, Adie SG, Chaney EJ, Marjanovic M, Tangella KV, Boppart SA. Three-dimensional optical coherence tomography for optical biopsy of lymph

nodes and assessment of metastatic disease. Ann Surg Oncol 2013;20: 3685–93.
35. Krouskop TA, Wheeler TM, Kallel F, Garra BS, Hall T. Elastic moduli of breast and prostate tissues under compression. Ultrason Imaging 1998;20:260–74.
36. Vakhtin AB, Kane DJ, Wood WR, Peterson KA. Common-path interferometer for frequency-domain optical coherence tomography. Appl Optics 2003;42:6953–8.
37. Kennedy BF, Liang X, Adie SG, Gerstmann DK, Quirk BC, Boppart SA, et al. *In vivo* three-dimensional optical coherence elastography. Opt Express 2011;19:6623–34.
38. Kennedy BF, Koh SH, McLaughlin RA, Kennedy KM, Munro PR, Sampson DD. Strain estimation in phase-sensitive optical coherence elastography. Biomed Opt Express 2012;3:1865–79.
39. Maintz J, Viergever MA. A survey of medical image registration. Med Image Anal 1998;2:1–36.
40. Cross SE, Jin Y-S, Rao J, Gimzewski JK. Nanomechanical analysis of cells from cancer patients. Nat Nanotechnol 2007;2:780–3.
41. Plodinec M, Loparic M, Monnier CA, Obermann EC, Zanetti-Dallenbach R, Oertle P, et al. The nanomechanical signature of breast cancer. Nat Nanotechnol 2012;7:757–65.
42. Buderer NMF. Statistical methodology: I. Incorporating the prevalence of disease into the sample size calculation for sensitivity and specificity. Acad Emerg Med 1996;3:895–900.
43. Kennedy BF, Malheiro FG, Chin L, Sampson DD. Three-dimensional optical coherence elastography by phase-sensitive comparison of C-scans. J Biomed Opt 2014;19:076006.
44. Olson T, Harter J, Munoz A, Mahvi D, Breslin T. Frozen section analysis for intraoperative margin assessment during breast-conserving surgery results in low rates of re-excision and local recurrence. Ann Surg Oncol 2007; 14:2953–60.
45. Wieser W, Biedermann BR, Klein T, Eigenwillig CM, Huber R. Multi-megahertz OCT: high quality 3D imaging at 20 million A-scans and 4.5 GVoxels per second. Opt Express 2010;18:14685–704.
46. Wang S, Larin K. Shear wave imaging optical coherence tomography (SWI-OCT) for ocular tissue biomechanics. Opt Lett 2014;39:41–4.
47. Crecea V, Oldenburg AL, Liang X, Ralston TS, Boppart SA. Magnetomotive nanoparticle transducersfor optical rheology of viscoelastic materials. Opt Express 2009;17:23114–22.
48. Kennedy KM, McLaughlin RA, Kennedy BF, Tien A, Latham B, Saunders CM, et al. Needle optical coherence elastography for the measurement of microscale mechanical contrast deep within human breast tissues. J Biomed Opt 2013;18:121510.
49. Li C, Guan G, Ling Y, Hsu Y-T, Song S, Huang JT-J, et al. Detection and characterisation of biopsy tissue using quantitative optical coherence elastography (OCE) in men with suspected prostate cancer. Cancer Lett 2015;357:121–8.